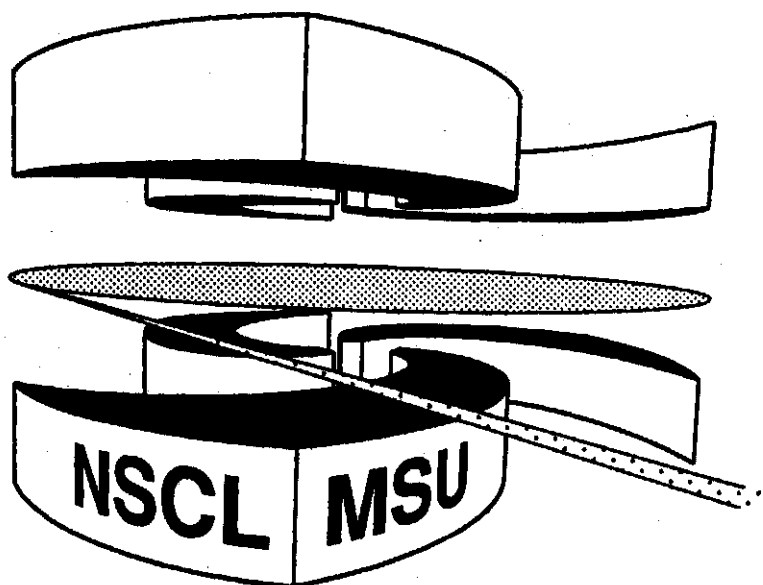# Michigan State University

National Superconducting Cyclotron Laboratory

TWO-FRAGMENT CORRELATION FUNCTIONS WITH DIRECTIONAL CUTS FOR CENTRAL ^{36}Ar + ^{197}Au COLLISIONS AT E/A = 50 MeV

T. GLASMACHER, L. PHAIR, D.R. BOWMAN, C.K. GELBKE, W.G. GONG, Y.D. KIM, M.A. LISA, W.G. LYNCH, G.F. PEASLEE, R.T. de SOUZA, M.B. TSANG, and F. ZHU

MSUCL-923

FEBRUARY 1994

Two-fragment correlation functions with directional cuts for central ^{36}Ar + ^{197}Au collisions at $E/A = 50$ MeV

T. Glasmacher, L. Phair', D.R. Bowman+, C.K. Gelbke, W.G. Gong*, Y.D. Kim§, M.A. Lisa', W.G. Lynch, G.F. Peaslee**, R.T. de Souza‡, M.B. Tsang and F. Zhu††

National Superconducting Cyclotron Laboratory and Department of Physics and Astronomy, Michigan State University, East Lansing, MI 48824, USA

(February 18, 1994)

Abstract

Two-fragment correlation functions observed in central collisions of ^{36}Ar + ^{197}Au at $E/A = 50$ MeV are compared to many-body trajectory calculations. For the present reaction, ambiguities between source size and lifetime can be reduced by employing directional emission cuts and describing observed differences between longitudinal and transverse correlation functions. For fragments emitted above the Coulomb barrier, $E/A \geq 6$ MeV, many-body Coulomb-trajectory calculations with a surface emission model indicate emission from an extended source of short lifetime.

PACS number: 25.70.Pq

I. INTRODUCTION

The emission of intermediate mass fragments (IMF) has been established as a decay mechanism of excited nuclear matter at high [1–3] and intermediate bombarding energies [4–12]. Some statistical treatments [13,14] are based upon the assumption of a nearly instantaneous fragmentation of an excited nuclear system at low density. Other models are based upon the assumption of a sequential decay mechanism from a hot and possibly expanding nuclear system undergoing equilibration between the individual binary disintegration steps [15,16]. Measurements of source dimensions and emission time scales can help determine which of these two extreme scenarios (if any) may be more realistic for the description of multifragment disintegrations.

Information about the space-time characteristics of the emitting system can be obtained via intensity interferometric techniques [17–22]. In the particular case of multifragment emission processes, one can explore two-fragment correlation functions [23–32]. Two-fragment correlations can be treated in terms of classical Coulomb trajectory calculations since the deBroglie wavelengths of the emitted particles are short and since final-state interactions are dominated by the long- range Coulomb interaction [26]. Correlations due to quantum statistics are negligible [43]. In general, the interaction of emitted fragments with the residual system cannot be neglected. Therefore, the interpretation of two-fragment correlation functions is generally based upon models employing three- or many- body Coulomb trajectory calculations [25–32].

Most analyses of two-fragment correlation functions employed correlation functions integrated over all angles between the total and relative momentum vectors of the emitted fragments (compatible with a given detector acceptance). Such "angle-integrated" correlation functions, cannot resolve certain ambiguities between source size and lifetime. Since fragment emission is believed to be enhanced if the systems can expand to subnormal density, the size of the fragment emitting source is unknown. Hence, the extracted lifetimes depend upon the assumed source geometry. In this paper, we will show that studies of longitudinal

and transverse correlation functions may help reduce such ambiguities. Specifically, we will reinvestigate two-fragment correlation functions measured [27,33] for the reaction ^{36}Ar + ^{197}Au at $E/A = 50$ MeV.

II. EXPERIMENTAL SETUP

The experiment was performed in the 92 inch scattering chamber of the National Superconducting Cyclotron Laboratory at Michigan State University. The K1200 cyclotron provided an ^{36}Ar beam of $E/A = 50$ MeV with an intensity of approximately 10^8 particles per second incident on a ^{197}Au target of about 1 mg/cm^2 thickness. Intermediate mass fragments and light charged particles in the angular range $9° \leq \theta_{lab} \leq 160°$ were detected with the MSU Miniball phoswich detector array [34], which covered approximately 89% of 4π in solid angle. This setup allowed atomic identification between $Z = 1$ and $Z = 18$ with energy thresholds between $E_{th}/A \approx 2$ MeV for $Z = 3$ and $E_{th}/A \approx 3$ for $Z = 10$ and $E_{th}/A \approx 4$ MeV for $Z = 18$ fragments. The energy calibrations for detectors in the forward rings between $\theta_{lab} = 9°$ and $\theta_{lab} = 40°$ are estimated to be accurate within 5%. Additional experimental details are given in Refs. [33,35].

III. EXPERIMENTAL CORRELATION FUNCTIONS

In this paper, we restrict ourselves to the analysis of two-fragment correlation functions observed in near-central collisions of ^{36}Ar + ^{197}Au at a beam energy of $E/A = 50$ MeV. These collisions were selected by cuts on the observed charged particle multiplicity, $N_C \geq 19$. This centrality cut corresponds to a reduced impact parameter [35,36] of $b/b_{max} \leq 0.3$, and it represents less than 10% of the reaction cross section. The average multiplicity of detected intermediate mass fragments in these central collisions was close to two [8,33].

For orientation, we present representative fragment energy spectra in Fig. 1. Left and right hand panels show spectra for beryllium and oxygen fragments, top and bottom panels show spectra measured in rings 2 and 4, centered at $\theta_{lab} = 19.5°$ and $\theta_{lab} = 35.5°$) of

the Miniball, respectively. Although the energy spectra resemble thermalized distributions, they are inconsistent with the assumption of isotropic thermal emission in a single source rest frame. Some nonequilibrium fragment emission is present even when the collisions are selected by central cuts [33,37]. The curves in Fig. 1 will be discussed further below.

Small angle correlation functions, $1 + R(\text{v}_{\text{red}})$, were constructed for pairs of intermediate mass fragments ($4 \leq Z_{\text{IMF}} \leq 9$), detected at angles between $16° \leq \theta_{\text{lab}} \leq 40°$ in the laboratory frame. The correlation function was defined as

$$1 + R(\text{v}_{\text{red}}) = C \frac{\sum Y_{12}(\mathbf{p_1}, \mathbf{p_2})}{\sum Y_{\text{back}}(\mathbf{p_1}, \mathbf{p_2})}, \tag{1}$$

where $Y_{12}(\mathbf{p_1}, \mathbf{p_2})$ is the measured coincidence yield and $Y_{\text{back}}(\mathbf{p_1}, \mathbf{p_2})$ is the "background yield" constructed via the event mixing technique. (Specifically, we mixed fragment yields from the previous five events.) In Eq. (1), $\mathbf{p_1}$ and $\mathbf{p_2}$ denote the laboratory momenta of the fragments 1 and 2, and v_{red} is the relative velocity of the particle pair defined as [25,26]

$$\text{v}_{\text{red}} = \frac{\text{v}_{\text{rel}}}{\sqrt{Z_1 + Z_2}} = \frac{\mathbf{p_1}/m_1 - \mathbf{p_2}/m_2}{\sqrt{Z_1 + Z_2}}. \tag{2}$$

All angle-integrated correlation functions presented in this paper are normalized to unity for large reduced velocities ($0.035c \leq \text{v}_{\text{red}} \leq 0.05c$) where the final state interaction between the fragments is small. The normalization constant determined from these angle-integrated correlation function was then used for the construction of directional correlation functions selected by cuts on the angle $\psi = \cos^{-1}\left[|\mathbf{P'}.\text{v}_{\text{red}}|/(P'v_{\text{red}})\right]$ between the reduced relative velocity vector, v_{red}, and the total momentum vector, $\mathbf{P'} = \mathbf{p'_1} + \mathbf{p'_2}$, of the coincident fragment pair, defined in the rest frame of an assumed source moving with a fixed velocity v_ψ parallel to the beam axis. (Nonrelativistically, $\mathbf{P'}$ depends on v_ψ, but v_{red} does not. Hence, ψ depends on v_ψ.) Longitudinal and transverse cuts were defined by $\psi_{\text{long}} = 0° - 50°$ and $\psi_{\text{trans}} = 80° - 90°$, respectively.

Angle-integrated correlation functions (no cut on ψ beyond the acceptance of the experimental apparatus) are shown in Fig. 2. The open points depict the correlation function constructed from fragments with energies above the detector threshold $E_{\text{lab}}/A = 3$ MeV;

the solid points depict the correlation function obtained with the additional software cut of $E_{lab}/A \geq 6$ MeV. These two cuts, $E_{lab}/A \geq 3$ and 6 MeV, are illustrated, by the dotted vertical lines in Fig. 1. The cut $E_{lab}/A \geq 6$ MeV primarily eliminates fragments emitted below the exit channel Coulomb barrier. The exclusion of low-energy fragments (with energies between $E_{lab}/A = 3 - 6$ MeV) manifests itself in an increased width of the Coulomb hole at small reduced velocities. Apparently, these very low-energy fragments experience a reduced mutual Coulomb repulsion. Qualitatively, such reduced final-state interactions could be caused by longer time scales for subbarrier emission of fragments or, alternatively, by fragment emission from the volume of an expanded dilute nuclear system [13,14] formed at the late stages of the reaction.

In Figure 3, longitudinal and transverse correlation functions (open points) are compared to angle-integrated correlation functions (solid points). The upper and lower panels show data selected by energy thresholds $E_{lab}/A \geq 3$ and 6 MeV, respectively. The directional cuts were defined close to the center-of-mass frame, $v_\psi = 0.04c$. (This specific choice of v_ψ has only a moderate influence on the shape of directional correlation functions, see also the discussion below.) The directional correlation functions reveal a surprising sensitivity to the applied energy threshold. The inclusion of low-energy fragments produces rather significant differences in the transverse and longitudinal correlation functions at small reduced velocities, $v_{red}/c \approx 0.01 - 0.02$. In addition, the longitudinal correlation function (open squares) exhibits a substantial change in shape and height at larger reduced velocities, $v_{red}/c \approx 0.02 - 0.05$. The differences at small v_{red} vanish when subbarrier emissions are excluded (lower panel), but the attenuation of the longitudinal correlation function at larger reduced velocities, $v_{red}/c \approx 0.02 - 0.05$, become even more pronounced.

The description of low-energy emissions ($E_{lab}/A = 3 - 6$ MeV) in terms of classical trajectory calculations is expected to be difficult. One may attempt modeling emission from the volume of a dilute nuclear system, or alternatively emission from an ensemble of sources containing a broad distribution of Coulomb barriers [38]. While such attempts may be interesting in their own right, they may be fraught with considerable ambiguity, especially

5

if barrier penetration effects which cannot be treated classically are important. Therefore, we will focus our analysis of the correlation functions on the data selected by the higher energy cut, $E_{lab}/A \geq 6$ MeV, for which the treatment of final-state interactions in terms of classical Coulomb trajectory calculations should be rather well justified.

IV. MANY-BODY TRAJECTORY CALCULATIONS

To extract size and lifetime parameters of emission sources consistent with the experimentally observed correlation functions, we simulated the final state interactions between the emitted fragments in terms of many-body trajectory calculations. For this purpose, the intermediate mass fragments were assumed to be sequentially emitted from the surface a spherical source of radius R_S, moving initially in beam direction with velocity $\mathbf{v}_S$. The source was assumed to consist of Z_S protons; its mass A_S was assigned to be that of the most abundant isotope. Charge, energy and angular distributions of the emitted fragments ($4 \leq Z_{IMF} \leq 9$) were selected by randomly sampling the experimental yield $Y(\mathbf{p})$. Examples of simulated energy spectra are shown in Fig. 1. For each charge number Z_{IMF}, the corresponding mass number A_{IMF} was assigned to be that of the most abundant isotope, and the radius of the emitted fragment was taken as $R_{IMF} = 1.2\,A_{IMF}^{1/3}$ fm. The emission times $t_i > 0$ for fragments i were assumed to follow an exponential probability distribution,

$$dP(t_i) = \frac{1}{\tau} e^{-t_i/\tau} |dt_i| \tag{3}$$

In this parametrization, the parameter τ represents the lifetime of the fragment emitting source or, alternatively, the average time interval between any two fragment emissions, $\langle |t_i - t_k| \rangle$. For events of fragment multiplicity N_{IMF}, the average time of emission of the first fragment is then given by $\langle t_1 \rangle = \tau/N_{IMF}$.

Specifically, in the rest-frame of the emitting source the emission function was assumed to have the form

$$g(\mathbf{p}', \mathbf{r}, t) \propto (\hat{\mathbf{r}} \cdot \hat{\mathbf{p}})\, \Theta(\hat{\mathbf{r}} \cdot \hat{\mathbf{p}})\, \delta(r - R_S - R_{IMF})\, \Theta(p^2 - 2mV_C)\, e^{-t/\tau}\, Y(\mathbf{p}). \tag{4}$$

6

where $Y(\mathbf{p})$ is the measured yield and $\mathbf{p}' = \mathbf{p}\sqrt{1 - 2mV_C/p^2}$ is the momentum of the emitted fragment at the point of emission $\mathbf{r}$ corrected for the average Coulomb repulsion V_C from the emitting source. Implications of this procedure on the energy spectra will be further discussed below.

In addition we imposed the requirement that each newly emitted fragment i had a minimum initial spatial separation of $r_{ij} \geq 1.2(A_i^{1/3} + A_j^{1/3})$ fm from all previously emitted particles j. Upon emission of a fragment the source recoils. The trajectories of the source, the newly emitted and all previously emitted particles under their mutual Coulomb intercation are calculated by numerically integrating Newton's equations of motion with an adaptive step-size Runge-Kutta algorithm [39]. This process is repeated till all fragments are emitted. The integration is terminated when the Coulomb energy between all pairs of particles becomes smaller than 0.1% of the relative kinetic energy between the same pairs of particles. The input parameters for this simulation are the source radius R_S, the initial source velocity v_S, the initial charge number Z_S, and the lifetime τ.

Between 1 and 4 million events were created for each simulation and written to disk [42]. These events were filtered for the geometrical acceptance, granularity, and energy thresholds of the MSU Miniball. (The only exceptions are the correlation functions in Fig. 8 where the effect of filtering is investigated.) The simulated and filtered events were then treated in exactly the same way as the measured data, and correlation functions were constructed as described in Sect. III.

V. COMPARISON BETWEEN DATA AND SIMULATIONS

Two–fragment correlation functions are sensitive to the strength of the final-state Coulomb interaction between the emitted fragments and also to the strength of the Coulomb interaction between emitted fragments and residual source [26]. Details of these final-state interactions depend on the source size and on the time-scale of fragment emission. In general, the correlations are reduced (i.e. the width of the minimum in the correlation function

at $v_{red} \approx 0$ becomes smaller) when the average separation between the emitted fragments becomes larger, as is the case for emission from larger sources or at larger time-intervals, see Figs. 4 and 5.

Figure 4 illustrates the dependence of the angle-integrated correlation function on the source radius R_S. In these calculations, the source was assumed to have a total charge of $Z_S = 40$ and to emit fragments on a very short time scale, $\tau = 10$ fm/c. The dashed, solid and dotted curves show correlation functions calculated for radii $R_S = 6, 10,$ and 14 fm, respectively. For a larger radius, the initial separation between the fragments is larger and the Coulomb repulsion between the emitted fragments is reduced, leading to a narrower Coulomb hole in the correlation function. The experimental correlation function can be reproduced by assuming emission from a very short-lived source of radius $R_S \approx 10$ fm.

Figure 5 illustrates the dependence of the angle-integrated correlation function on the emission time scale. In these calculations, fragments were assumed to be emitted from a source of total charge $Z_S = 40$ and radius $R_S = 6$ fm. The dotted, solid, dot-dot-dashed, and dashed curves show correlation functions calculated for $\tau = 10, 75, 125,$ and 200 fm/c, respectively. A larger emission time translates into a larger initial separation between the fragments, resulting in weaker final-state interactions between the emitted fragments and, hence, a smaller Coulomb hole in the correlation function. The experimental correlation function can also be reproduced by assuming emission from a small source of radius $R_S \approx 6$ fm and finite lifetime $\tau \approx 75$ fm/c. While angle-integrated two-fragment correlation functions are sensitive to the space-time characteristics of the emitting system, they are poorly fit to distinguish between emission from larger, but short-lived sources as opposed to emission from small, but longer-lived sources. This ambiguity is illustrated more clearly in Fig. 6. Four different combinations of radius and lifetime, ranging from $(R_S, \tau) = (10$ fm, 10 fm/c$)$ to $(R_S, \tau) = (5.5$ fm, 100 fm/c$)$, predict virtually indistinguishable angle-integrated two-fragment correlation functions. Hence, for the present source parametrization, the accuracy of lifetime determination is limited by uncertainties of the source radius. In spite of this ambiguity, the measured correlation function indicates a short emission time scale, $\tau \leq 100$

fm/c, for all reasonable source dimensions, thus corroborating the conclusions reached by previous analyses [25–28,30] of multifragment emission processes at comparable energies.

The space-time ambiguity can be reduced by employing directional cuts in the construction of the two-fragment correlation function which are more sensitive to the mutual interactions between the two detected fragments and the emitting source, i.e. by constructing correlation functions for pairs of fragments with their relative velocity mainly parallel or transverse to their total momentum vector. Similar cuts (but for different physics reasons) can been employed [40] to obtain independent size and lifetime information from two-proton correlation function measurements. For the case of two-fragment correlation functions, directional cuts were shown to contain additional information about the geometrical configuration of the fragmenting system [41].

Measured (solid points) and calculated (curves) longitudinal two-fragment correlation functions are compared in Fig. 7. The calculations illustrate that longitudinal correlation functions are non-degenerate for the same sets of parameters from Fig. 6 which produced nearly indistinguishable angle-integrated correlation functions. This suggests that simultaneous investigation of angle-integrated and directional correlation functions can reduce the ambiguities encountered in the interpretation of angle-integrated correlation functions alone. (Transversal correlation functions display much less sensitivity and are not shown here.) With increasing lifetime, the calculated longitudinal correlation function becomes flatter for $0.01 \leq v_{red}/c \leq 0.03$, and then exhibits a more gradual rise towards unity at larger values of v_{red}. (While the longitudinal correlation functions do not reach unity for the reduced velocity range plotted here, we have verified that they do approach unity for larger reduced velocities, $v_{red} \approx 0.1c$.)

The experimental data fall within the range spanned by the simulations and agree best with the calculations for $(R_S, \tau) = (8 \text{ fm}, 50 \text{ fm}/c)$, indicating fragment emission on a fast time scale and from a rather large source. In the following we will investigate how stable the simulations are with respect to variations in uncertain model assumptions and parameters.

First we examine the influence of distortions from the experimental apparatus by filtering

9

the simulations through a software replica of the detector in Fig. 8. For these calculations, the parameters $R_S = 10$ fm, $\tau = 10$ fm/c were chosen. To illustrate the origin and magnitude of instrumental distortions, the dashed curves depict correlation functions gated on specific ranges of ψ and predicted for an ideal detector (perfect energy and angular resolution), with events filtered only by the overall angular acceptance of $16° \leq \theta_{\mathrm{lab}} \leq 40°$ and the applied detection threshold of $E_{\mathrm{lab}}/A \geq 6$ MeV. To assess effects of finite energy resolution and uncertainty in individual detector calibrations, we simulated correlation functions by assuming a kinetic energy resolution function of Gaussian shape and variance $\sigma = E_{\mathrm{lab}}/4$. This uncertainty is much larger than the estimated uncertainty in energy calibration (5%). The solid curves show results of these simulations (still assuming perfect angular resolution). The similarity of the solid and dashed curves shows that energy resolution effects are largely negligible. The points represent fully filtered two-fragment correlation functions for which the additional distortions due to the finite granularity of the array are taken into account. (Results of such fully filtered calculations are compared to the measured correlation functions in all other figures.) The finite granularity of the detector causes only minor distortions of the angle-integrated and transverse correlation functions, but somewhat larger distortions of the longitudinal correlation function which suffers an additional suppression for $v_{\mathrm{red}} \geq 0.02c$. Since the determination of the lifetime depends both on the slope and on the magnitude of the longitudinal correlation function, the finite granularity of the detection apparatus must be taken into account carefully.

Nonrelativistically, v_{red} is independent of the source velocity, but the total momentum $\mathbf{P'}$ in the chosen rest frame and the angle ψ are not. In our analysis, we assumed a source velocity of $v_S = 0.04c$ and used the same velocity to define the longitudinal and transverse cuts in this rest frame, i.e. we assumed $v_S = v_\psi$. (The velocity of the center-of-mass frame for ^{36}Ar + ^{197}Au at $E/A = 50$ MeV is 0.05c. We chose a slightly smaller velocity to take the momentum carried away by preequilibrium particle emission into account.) To explore the sensitivity of the extracted longitudinal and transverse correlation functions on the specific choice of v_ψ, we investigated other scenarios in which directional cuts were defined in rest

frames of velocities $v_\psi = 0$ and 0.08c. The experimental correlation functions extracted with angular cuts in these alternative rest frames are compared in the top panel of Fig. 9. The resulting differences are small. Simulations performed for a source with the same parameters as in Fig. 8 ($Z_S = 40, R_S = 10$ fm/c, $\tau = 10$ fm/c) are shown in the bottom panel of the figure. They exhibit the same trend as the data. We conclude that our specific choice of v_ψ introduces little uncertainty, especially when data and calculations are treated consistently.

The numerical trajectory simulations assume an emitting system of initial velocity v_S. Since the source velocity is not known, we adopt a source velocity of $v_S = 0.04c$ which is close to the fusion velocity, $v_{\text{fusion}} = 0.05c$. This choice is consistent with that made in Refs. [25–28,30]. Angle-integrated as well as longitudinal correlation functions were found to be rather insensitive to the particular choice of source velocity over the range from $v_S = 0.0$ (corresponding to emission from a heavy target residue at rest in the laboratory) to $v_S = 0.05c$ (corresponding to emission from a completely fused compound nucleus). For central collisions, source velocities much larger than v_{fusion} are unphysical. Indeed, simulations performed for $Z_S = 40$ and $v_S = 2\,v_{\text{fusion}}$ encountered serious difficulties in reproducing the low-energy portion of the measured kinetic energy spectra leading to sizable distortions in the longitudinal correlation function.

In order to address uncertainties arising from the unknown charge of the emitting source, we simulated emission from sources ($v_S = 0.04c$) of fixed radius and lifetimes ($R_S = 7$ fm, $\tau = 10$ fm/c), but different charge numbers. Angle-integrated correlation functions for charge numbers of ZS = 40, 60, and 79 are shown in Fig. 10 by the solid, dashed, and dotted curves, respectively. The angle-integrated correlation functions become slightly steeper with increasing charge. Best agreement with the data is obtained for $Z_S = 40$.

While the influence of the initial charge on the angle-integrated correlation function is small, it clearly affects the low-energy portion of the simulated energy spectra, see the examples shown Fig. 1. For the smaller initial charge ($Z_S = 40$), the calculated energy spectra agree well with the data at energies $E/A \geq 6$ MeV, with some minor deviation occurring at energies slightly below the Coulomb barrier. For an initial charge of $Z_S = 79$,

however, it becomes impossible in this classical surface emission model to simulate the energy spectra properly, since subbarrier emission is not included. The energy spectra simulated for $Z_S = 79$ deviate from the experimental spectra up to energies well above the Coulomb barrier. This is, however, the region where most of the experimental yield is detected. Simulations for $Z_S = 79$, must therefore be viewed with caution.

Significant differences can also be detected in the reduced velocity distributions of coincident fragments (top panels of Fig. 11) and of the background yield (bottom panels of Fig. 11) constructed via the mixed event technique. The solid points in Fig. 11 show the experimental reduced velocity distributions; relative velocity distributions calculated for $Z_S = 40$ (left panels) and $Z_S = 79$ (right panels) are shown by the curves. The simulations for $Z_S = 40$ agree better with the data than those for $Z_S = 79$.

In view of the discrepancies between data and simulations for $Z_S = 79$, and of the much better agreement for $Z_S = 40$, we discard the simulations for $Z_S = 79$ as unrealistic. However, some uncertainty concerning the choice of Z_S remains. In Fig. 12, longitudinal (open points) and angle-integrated (solid points) correlation functions are compared to calculations for $Z_S = 40$ and 60. The larger initial charge of $Z_S = 60$ causes a small upward shift in the longitudinal correlation function. One possible explanation for this reduced value of charge is pre-equilibrium emission of charged particles. If one takes this explanation seriously and combines $Z_S = 60$ with the previously extracted best fits for radius and lifetime, $(R_S, \tau) = (8$ fm, 50 fm/c), one can obtain a rough estimate of the average density of the reaction zone. Assuming a neutron to proton ratio of 1.4, $Z_S = 60$, and a source radius of $R_S \approx 8$ fm, the density of the reaction zone may be estimated to be of the order of $\rho/\rho_0 \approx 0.4$. In view of the rather simple model assumptions employed in our analysis (neglect of volume emission and of nonspherical source shapes) and in view of the limited statistical accuracy of experimental data, the extracted source density must be viewed with some caution. Nevertheless, the data suggest fragment emission from an expanded (and hence dilute) source.

Finally, we wish to point out that firm conclusions can only be arrived at if the trajectory calculations provide a realistic description of the fragment energy spectra. Figure 13

illustrates this point. The figure shows longitudinal and transverse two-fragment correlation functions predicted for emission from the surface of a highly charged source of $Z_S = 79$, radius $R_S = 7$ fm and lifetime $\tau = 75$ fm/c. (For this source, neither the low-energy portion of the fragment energy spectra, nor the relative velocity distributions of coincident fragments were reproduced, see Figs. 1 and 11.) For such a highly charged source, the Coulomb barrier is too high to allow for significant fragment emission below $E/A \approx 6$ MeV. Hence, virtually identical correlation functions are predicted for the thresholds $E/A \geq 3$ and 6 MeV. The predicted longitudinal (dashed line) and transverse (dotted line) correlation functions exhibit shape changes relative to the angle-integrated (solid line) correlation function which are qualitatively similar to those observed in the data for $E/A \geq 3$ MeV (see top panel of Fig. 3). In contrast to the calculations, this shape change disappears in the data when raising the threshold to $E/A \geq 6$ MeV.

Within the present model, we have not been able to find a consistent and satisfactory explanation for the low-energy ($E/A \geq 3$ MeV) longitudinal and transverse correlation functions shown in the upper panel of Fig. 3. Two-fragment correlation functions for emission near and below the sharp-sphere Coulomb barrier are likely to be increasingly sensitive to many-body Coulomb interactions between the emitted fragments and hence to the geometrical configuration at breakup [41]. Realistic modeling should include emission from the volume of the dilute reaction zone and possibly nonspherical shapes. Future studies of such correlation functions in terms of microscopic models for fragment production allowing more realistic treatments of fragment emission from the volume of a dilute nuclear matter distribution might provide important additional insight.

VI. SUMMARY

We have studied two-fragment correlation functions for intermediate mass fragments emitted above the Coulomb barrier in central reactions of ^{36}Ar + ^{197}Au at $E/A = 50$ MeV. The correlation functions were analyzed by simulating the emission of fragments from the

surface of a spherical source of radius R_S and lifetime τ, and by treating final state interactions by means of many-body Coulomb trajectory calculations. Angle-integrated correlation functions were shown to exhibit significant ambiguities with regard to the parameters R_S and τ, with nearly equivalent correlation functions being predicted for emission from a large but short-lived source ($R_S = 10$ fm, $\tau = 10$ fm/c) and a small but longer lived source ($R_S = 5.5$ fm, $\tau = 100$ fm/c). This ambiguity is reduced for longitudinal correlation functions. A consistent description of both angle–integrated and longitudinal correlation functions could be achieved by assuming emission on a fast time scale form the surface of an extended spherical source. The extracted average time for the emission of *all* fragments is $\tau \approx 50$ fm/c with a corresponding radius of $R_S \approx 8$ fm.

ACKNOWLEDGEMENTS

REFERENCES

* Present address: Lawrence Berkeley Laboratory, Berkeley, CA 94720, USA.

† Present address: Chalk River Laboratories, Chalk River, Ontario K0J 1J0, Canada.

‡ Present address: Indiana University Cyclotron Facility, Bloomington, IN 47405.

§ Present address: National Laboratory for High Energy Physics, 1-1 Oho, Tsukuba, Ibaraki 305, Japan.

** Present address: Physics Department, Hope College, Holland, MI 49423.

†† Present address: Brookhaven National Laboratory, Upton, NY 11973.

[1] J. W. Harris *et al.*, Nucl. Phys. **A471**, 241c (1987).

[2] C. A. Ogilvie *et al.*, Phys. Rev. Lett. **67**, 1214 (1991).

[3] J. P. Alard *et al.*, Phys. Rev. Lett. **69**, 889 (1992).

[4] Y. D. Kim *et al.*, Phys. Rev. Lett. **63**, 494 (1989).

[5] Y. Blumenfeld *et al.*, Phys. Rev. Lett. **66**, 576 (1991).

[6] E. Piasecki *et al.*, Phys. Rev. Lett. **66**, 1291 (1991).

[7] D. R. Bowman *et al.*, Phys. Rev. Lett. **67**, 1527 (1991).

[8] R. T. de Souza *et al.*, Phys. Lett. **B268**, 6 (1991).

[9] K. Hagel *et al.*, Phys. Rev. Lett. **68**, 2141 (1992).

[10] B. Lott *et al.*, Phys. Rev. Lett. **68**, 3141 (1992).

[11] T. C. Sangster *et al.*, Phys. Rev. C **46**, 1404 (1992).

[12] D. R. Bowman *et al.*, Phys. Rev. C **46**, 1834 (1992).

[13] J. Bondorf, R. Donangelo, I. Mishustin, and H. Schulz, Nucl. Phys. **A444**, 460 (1985).

[14] D. Gross, Z. Xiao-ze, and X. Shu-yan, Phys. Rev. Lett. **56**, 1544 (1986).

[15] W. A. Friedman and W. G. Lynch, Phys. Rev. C **28**, 16 (1983).

[16] W. A. Friedman, Phys. Rev. Lett. **60**, 2125 (1988).

[17] S. E. Koonin, Phys. Lett. **B70**, 43 (1977).

[18] S. Pratt and B. Tsang, Phys. Rev. C **36**, 2390 (1987).

[19] T. C. Awes *et al.*, Phys. Rev. Lett. **61**, 2665 (1988).

[20] G. F. Bertsch, Nucl. Phys. **A498**, 173c (1989).

[21] D. H. Boal, C. K. Gelbke, and B. K. Jennings, Rev. Mod. Phys. **62**, 553 (1990).

[22] W. Bauer, G. F. Bertsch, and H. Schulz, Phys. Rev. Lett. **69**, 1888 (1992).

[23] R. Trockel *et al.*, Phys. Rev. Lett. **59**, 2844 (1987).

[24] R. Bougault *et al.*, Phys. Lett. **B232**, 291 (1989).

[25] Y. D. Kim *et al.*, Phys. Rev. Lett. **67**, 14 (1991).

[26] Y. D. Kim *et al.*, Phys. Rev. C **45**, 387 (1992).

[27] D. Fox *et al.*, Phys. Rev. C **47**, R421 (1993).

[28] E. Bauge *et al.*, Phys. Rev. Lett. **70**, 3705 (1993).

[29] T. C. Sangster *et al.*, Phys. Rev. C **47**, R2457 (1993).

[30] D. R. Bowman *et al.*, Phys. Rev. Lett. **70**, 3534 (1993).

[31] T. Ethvignot *et al.*, Phys. Rev. C **48**, 618 (1993).

[32] B. Kämpfer *et al.*, Phys. Rev. C **48**, R955 (1993).

[33] L. Phair, Ph.D. thesis, Michigan State University, 1993.

[34] R. T. de Souza *et al.*, Nucl. Instrum. Methods **A295**, 109 (1990).

[35] L. Phair *et al.*, Nucl. Phys. **A548**, 489 (1992).

[36] L. Phair *et al.*, Nucl. Phys. **A564**, 453 (1993).

[37] Y. D. Kim *et al.*, Phys. Rev. C **45**, 338 (1992).

[38] D. J. Fields *et al.*, Phys. Rev. C **34**, 536 (1986).

[39] W. H. Press, S. A. Teuolsky, W. T. Vetterling, and B. P. Flannery, *Numerical Recipes in Fortran*, 2nd ed. (Cambridge University Press, 1992).

[40] M. A. Lisa *et al.*, Phys. Rev. Lett. **71**, 2863 (1993).

[41] T. Glasmacher, C. K. Gelbke, and S. Pratt, Phys. Lett. **B314**, 265 (1993).

[42] The creation of 1 million events takes about 6 CPU hours on a DEC 3000/400 computer.

[43] Correlations due to quantum symmetry occur on a length scale comparable to the Bohr radius r_B. For intermediate mass fragments r_B is much smaller than their classical radius.

17

FIG. 1. Energy spectra of beryllium (left side) and oxygen (right side) nuclei emitted in central $^{36}Ar + {}^{197}Au$ collisions ($b/b_{max} \leq 0.3$) at $E/A = 50$ MeV observed in ring 2 (top panels) and ring 4 (bottom panels) of the MSU Miniball detector. The experimental spectra are shown as solid points; the simulated energy spectra ($R_S = 7$ fm, $\tau = 75$ fm/c) after filtering are plotted as solid, dash–dotted and dashed curves for three different initial source charges $Z_S = 40$ ($A_S = 90$), $Z_S = 60$ ($A_S = 142$) and $Z_S = 79$ ($A_S = 197$). The dotted vertical lines indicate the energy thresholds of $E_{th}/A = 3$ and 6 MeV.

FIG. 2. Measured angle-integrated fragment-fragment correlation functions for charges ($4 \leq Z_{IMF} \leq 9$) emitted in central $^{36}Ar + {}^{197}Au$ collisions ($b/b_{max} \leq 0.3$) at $E/A = 50$ MeV. The correlation functions are shown for fragments detected at forward angles ($16° \leq \theta_{lab} \leq 40°$). Energy thresholds of $E_{th} > 6$ MeV/nucleon (solid points) and $E_{th} > 3$ MeV/nucleon (open points) are applied to each fragment in the laboratory frame. The experimental error bars are smaller than the size of the plotted symbols.

FIG. 3. Measured directional IMF-IMF correlation functions for the constraints on fragment energies indicated in panels (a) and (b). Longitudinal (squares) and transverse (diamonds) correlation functions correspond to $\psi_{long} = 0° - 40°$ and $\psi_{trans} = 80° - 90°$ measured in a rest frame of velocity $v_\psi = 0.04c$.

FIG. 4. Angle-integrated correlation functions simulated via many-body Coulomb trajectory calculations (described in the text) for different source radii R_S (lines). The measured correlation function is shown by solid points. The simulations are filtered for acceptance, detector granularity, and energy thresholds.

FIG. 5. Angle-integrated correlation functions simulated via many-body Coulomb trajectory calculations (described in the text) for different source lifetimes τ (lines). The measured correlation function is shown by solid points. The simulations are filtered for acceptance, detector granularity, and energy thresholds.

FIG. 6. Angle-integrated correlation functions simulated with the four different parameter sets (indicated in the figure) are virtually indistinguishable.

FIG. 7. Longitudinal correlation functions ($\psi = 0° - 40°$, $v_\psi = 0.04c$) can reduce the ambiguities shown in Fig. 6.

FIG. 8. Illustration of instrumental distortions for correlation functions calculated with source the parameters ($\tau = 10$ fm/c, $R_S = 10$ fm, $Z_S = 40$). Symbols represent fully filtered correlation functions. The correlation functions shown as lines assume perfect angular resolution; dashed lines show the response for perfect energy resolution and solid lines show the response for a detector of much poorer energy resolution than estimated for the Miniball. For each curve, the gate on ψ is identical to the one imposed on the fully filtered correlation function shown in symbols closest to the curve. Additional details are given in the text.

FIG. 9. Directional correlation functions analyzed in two different rest frames. The solid and open points in the top panel show results obtained for $v_\psi = 0$ and $v_\psi = 0.08c$, respectively. The bottom panel depicts correlation functions simulated for a source of initial velocity $v_S = 0.04c$ but analyzed assuming $v_\psi = 0$ (solid curves) and $v_\psi = 0.08c$ (dashed curves), respectively. (Since angle-integrated correlation functions ($0° \leq \psi \leq 90°$) are independent of v_ψ the open and solid circles in panel (a) as well as the solid and dashed lines for the all-directional cut in panel (b) coincide.)

FIG. 10. Angle-integrated correlation functions calculated for different assumptions about the initial charge of the source Z_S. Solid, dashed and dotted curves depict calculations for $Z_S = 40$, 60 and 79 ($A_S = 90$, 142 and 197). Measured correlation function are shown by solid points.
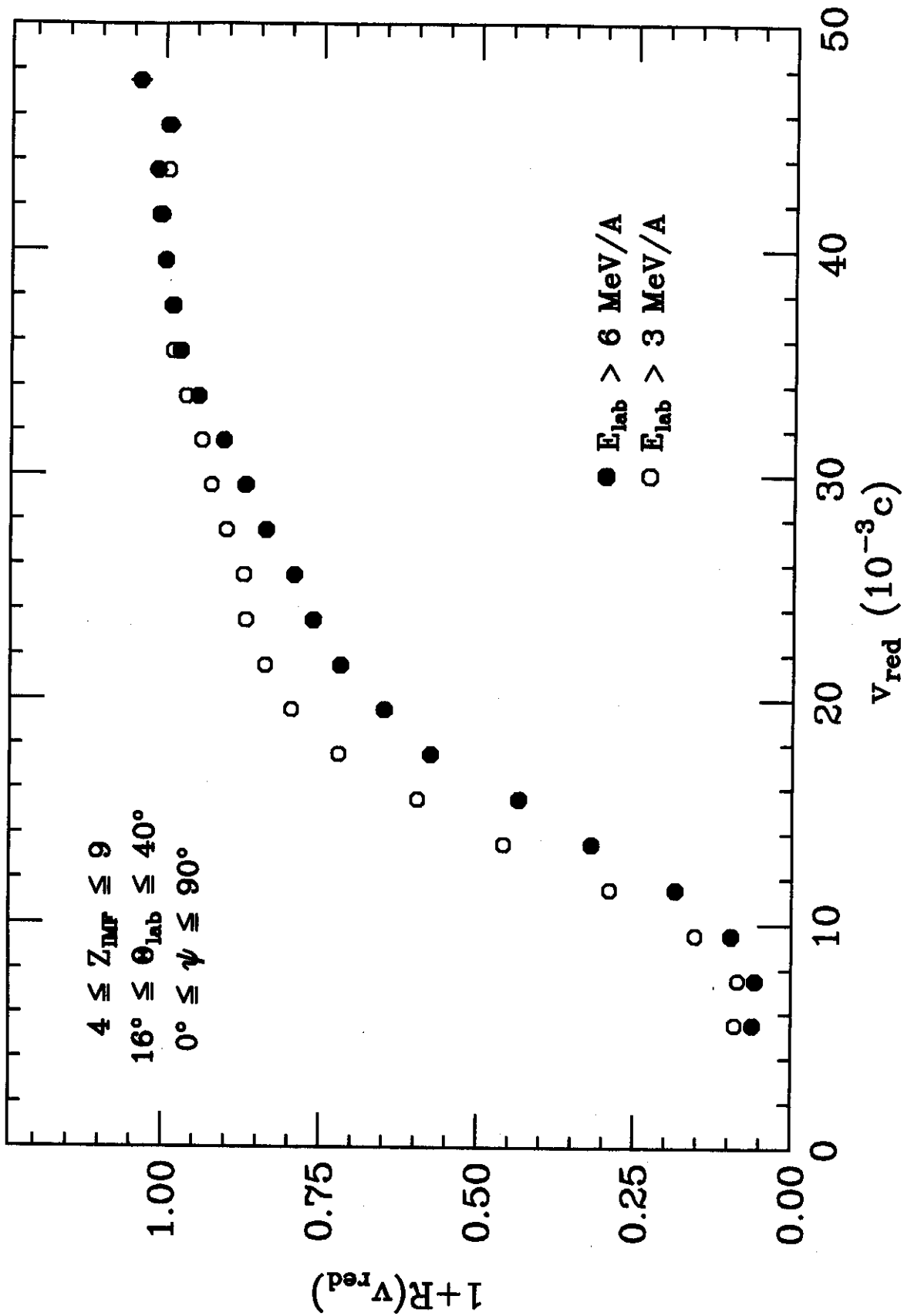
FIG. 11. Reduced relative velocity distributions $Y_{12}(v_{\text{red}})$ (top panels) and corresponding background spectra $Y_{\text{back}}(v_{\text{red}})$ (bottom panels) obtained via the mixed event technique from a source with $(R_S, \tau) = (7$ fm, 75 fm/c). The solid and dashed curves show results of simulations for $Z_S = 40$ and 79, respectively. Data are shown by solid points.
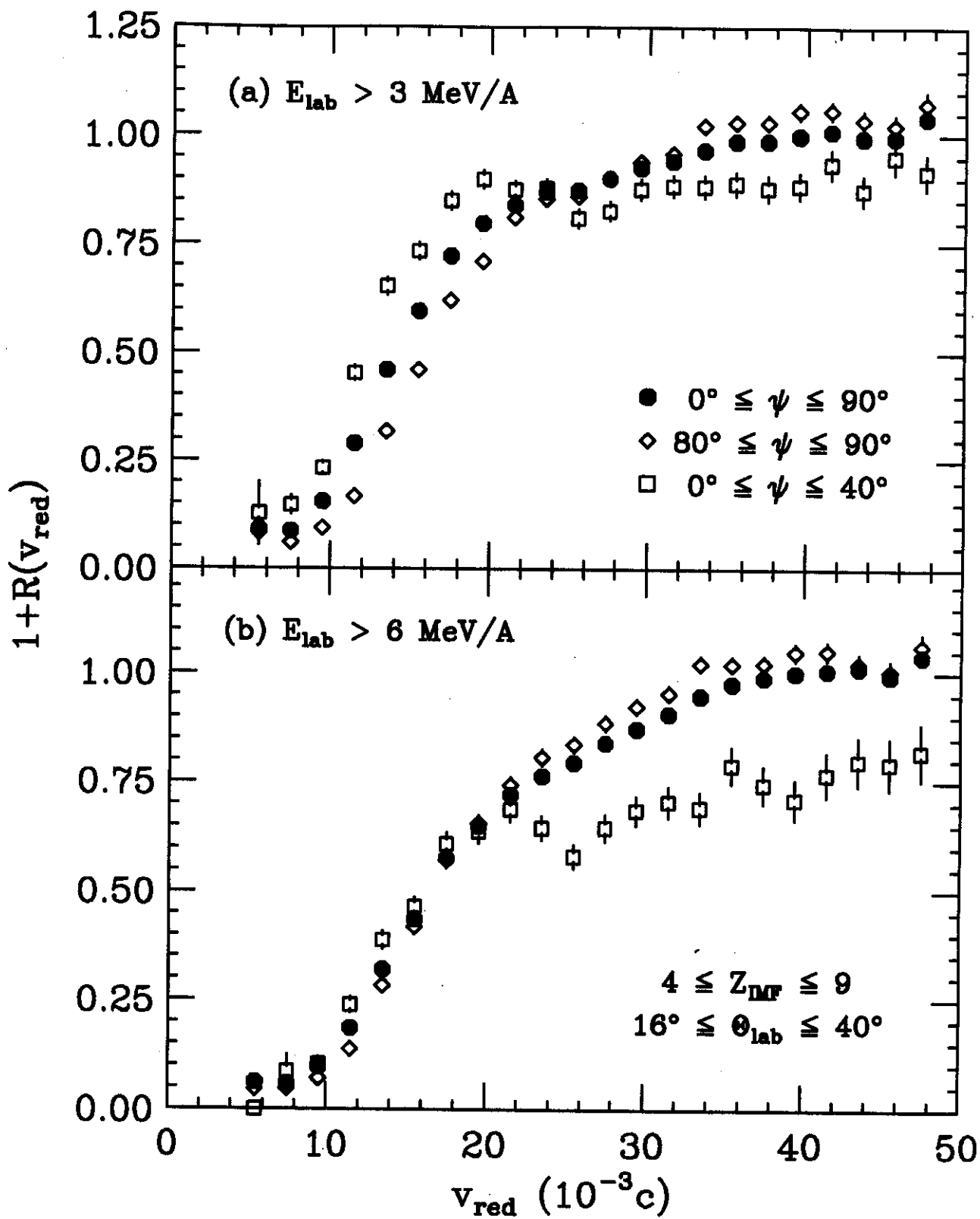
FIG. 12. Simulated angle-integrated and longitudinal correlation functions for charges $Z_S = 40$ (solid curves) and $Z_S = 60$ (dashed curves). The data are shown as points. For each curve, the gate on ψ is identical to the one imposed on the experimental correlation function shown in symbols closest to the curve.

FIG. 13. Longitudinal (dashed line), transverse (dotted line) and angle integrated (solid line) two-fragment correlation functions predicted for emission from the surface of a highly charged source of $Z_S = 79$, radius $R_S = 7$ fm and lifetime $\tau = 75$ fm/c.
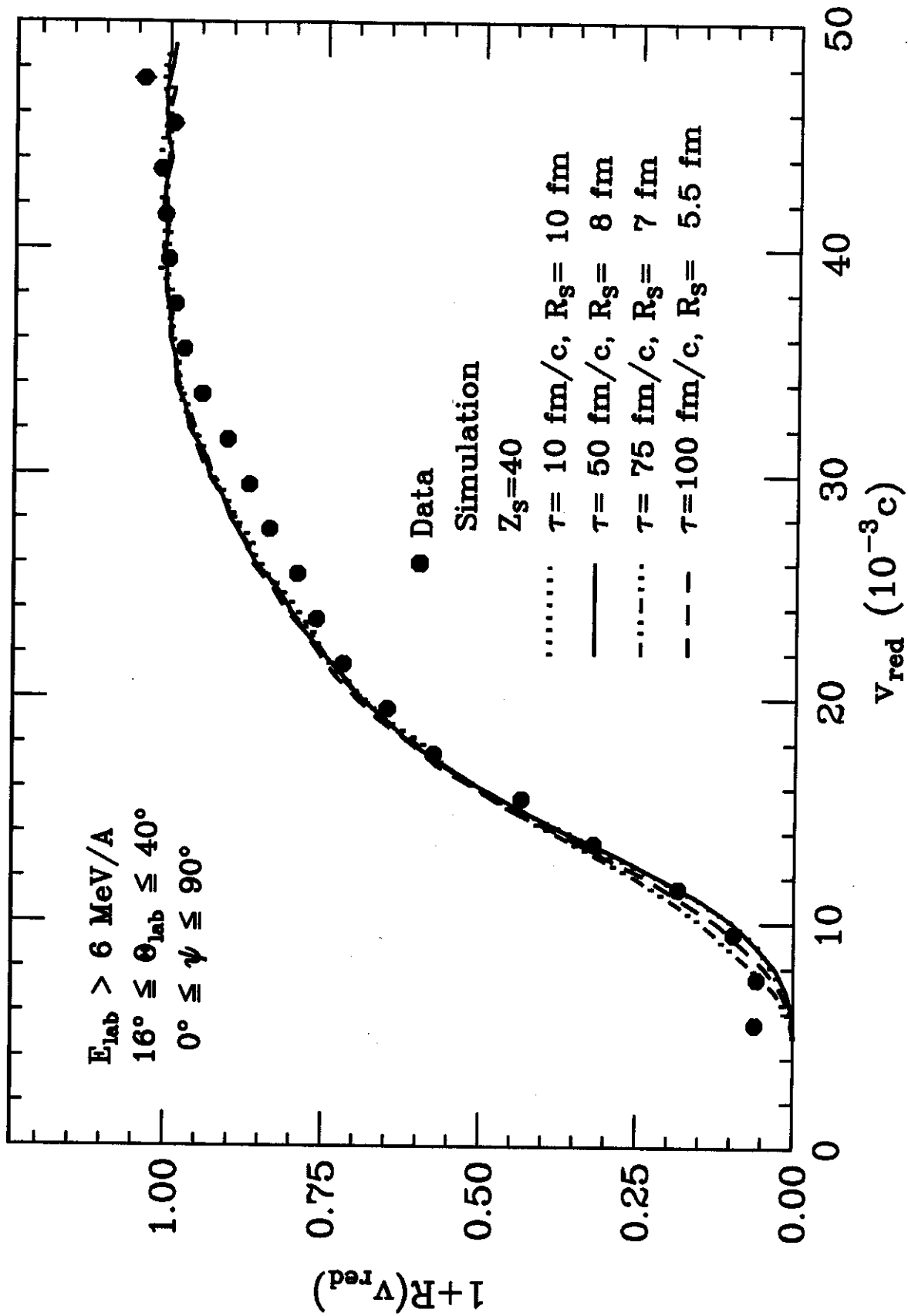
Glasmacher – Figure 1

$4 \leq Z_{IMF} \leq 9$
$16° \leq \theta_{lab} \leq 40°$
$0° \leq \psi \leq 90°$

● $E_{lab} > 6$ MeV/A
○ $E_{lab} > 3$ MeV/A

v_{red} ($10^{-3}c$)

$1+R(v_{red})$

Glasmacher – Figure 2

(a) $E_{lab} > 3$ MeV/A

$0° \leq \psi \leq 90°$
$80° \leq \psi \leq 90°$
$0° \leq \psi \leq 40°$

(b) $E_{lab} > 6$ MeV/A

$4 \leq Z_{IMF} \leq 9$
$16° \leq \Theta_{lab} \leq 40°$

v_{red} $(10^{-3}c)$

$1 + R(v_{red})$
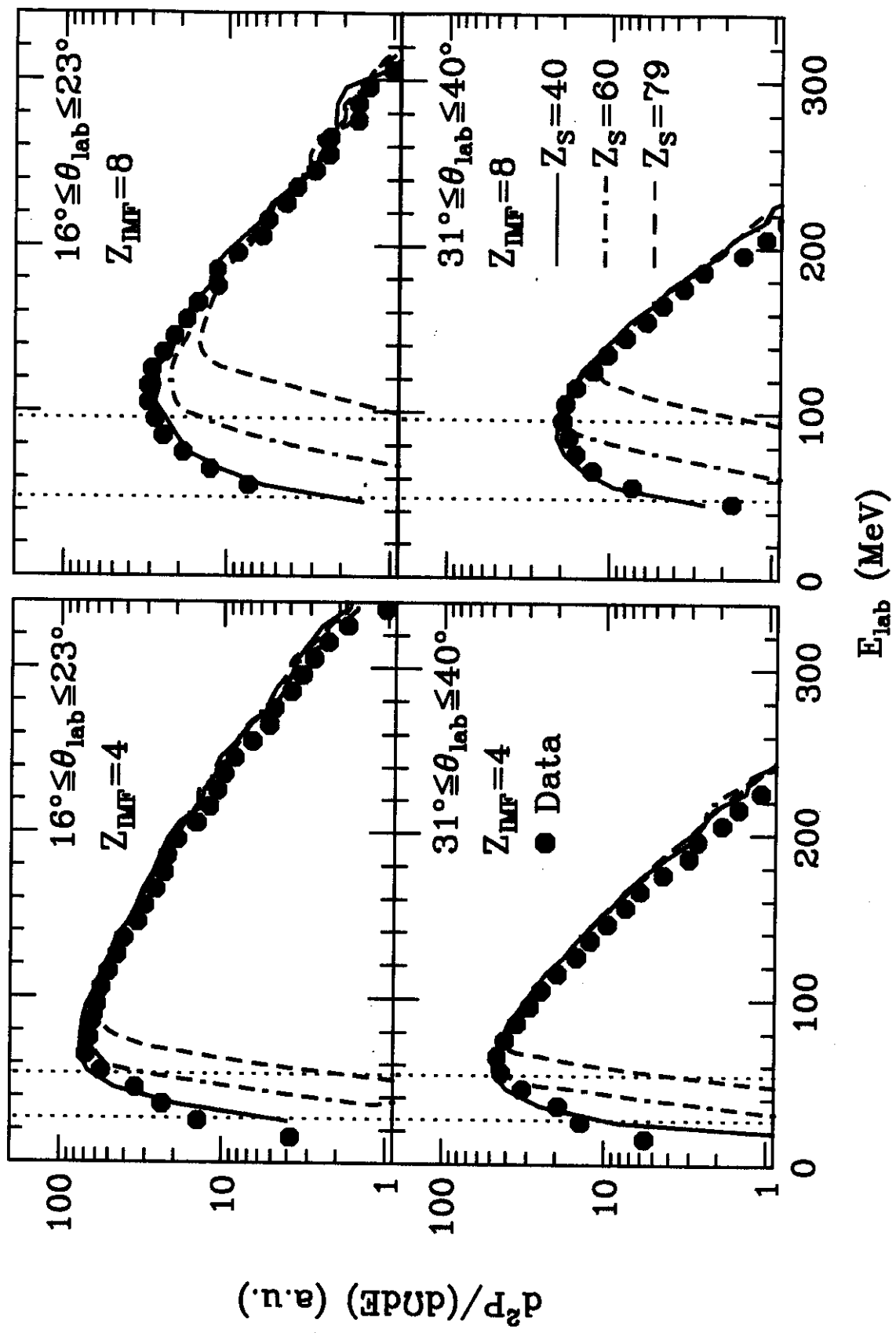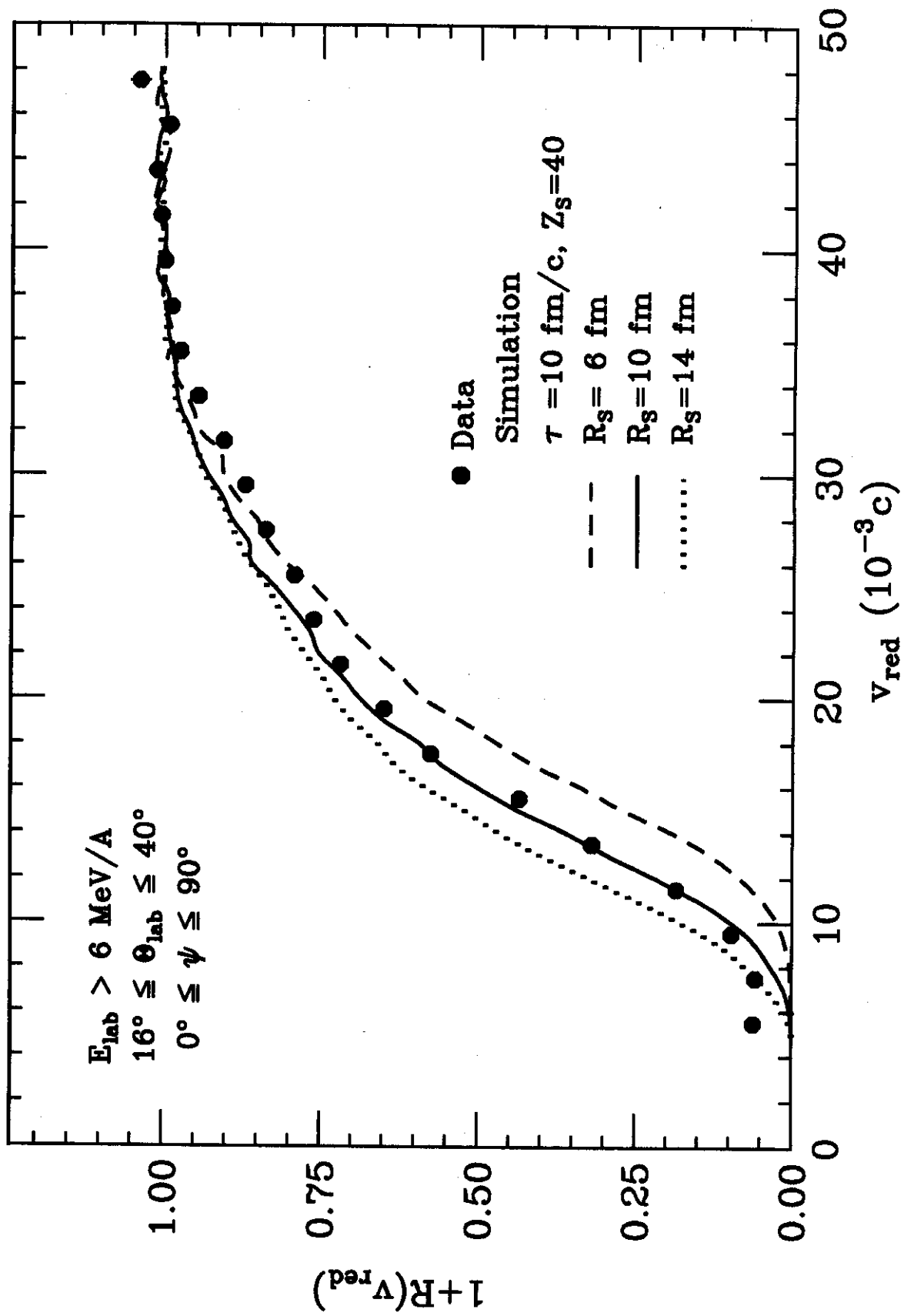
Glasmacher -- Figure 4
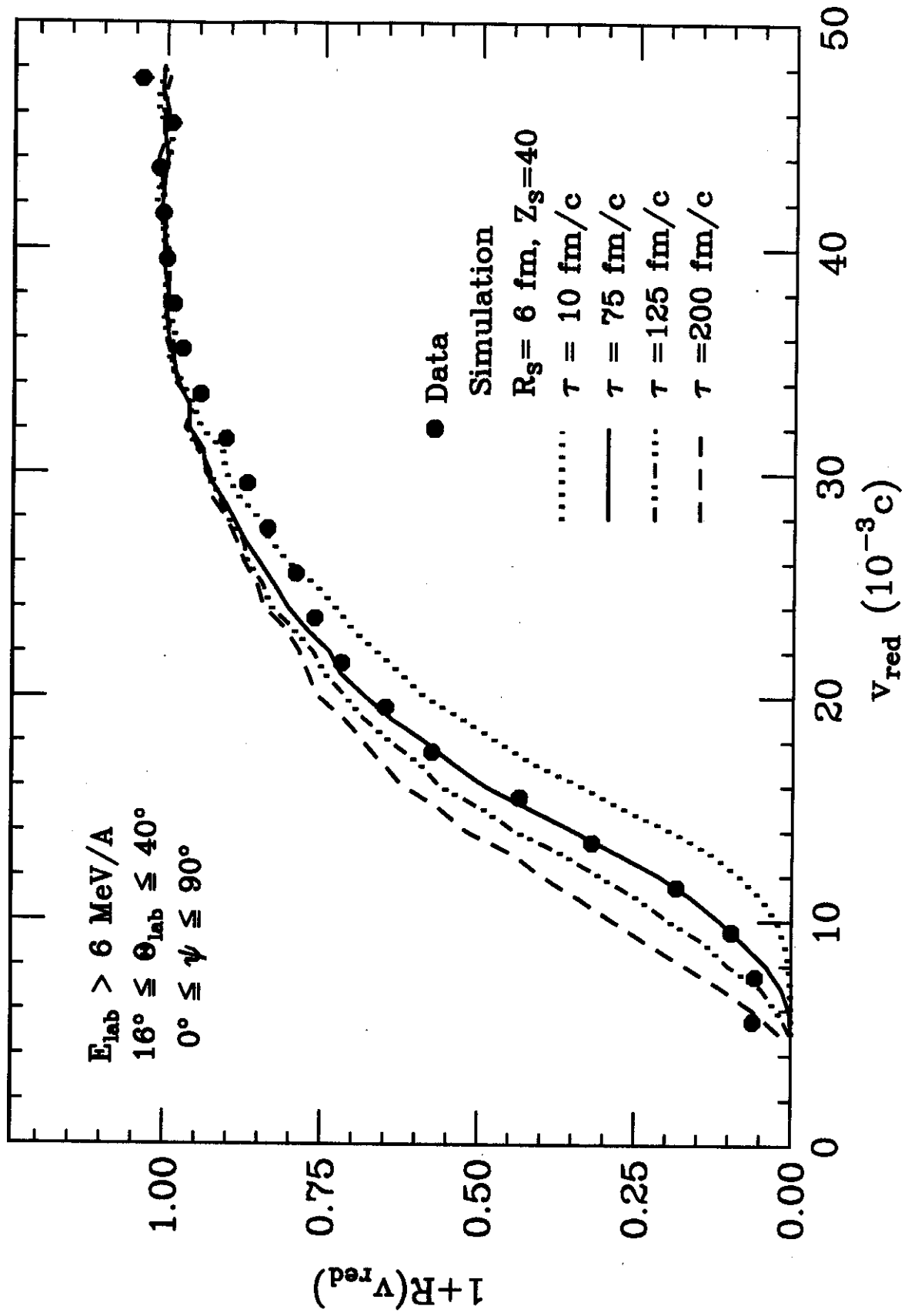
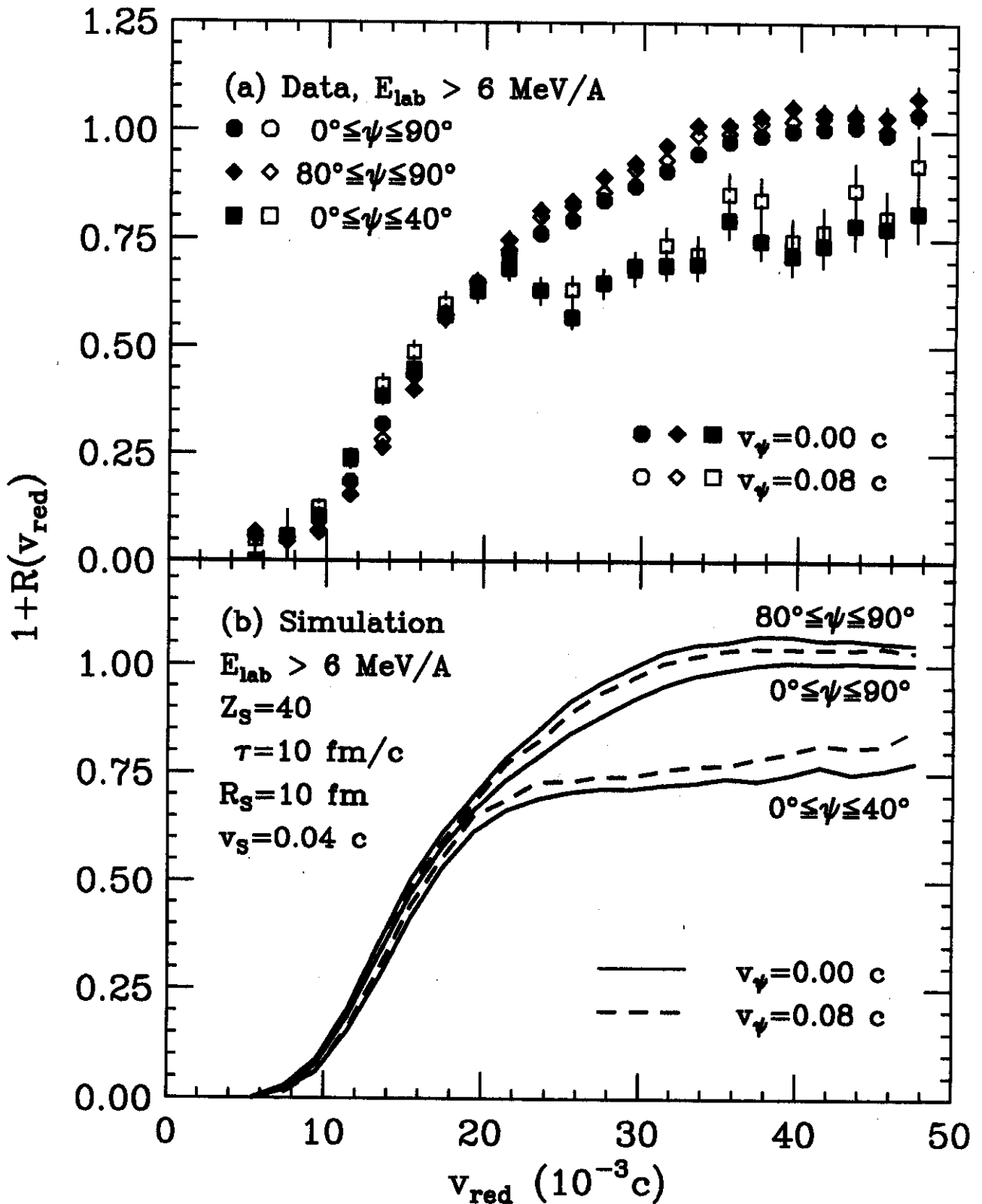Glasmacher – Figure 5
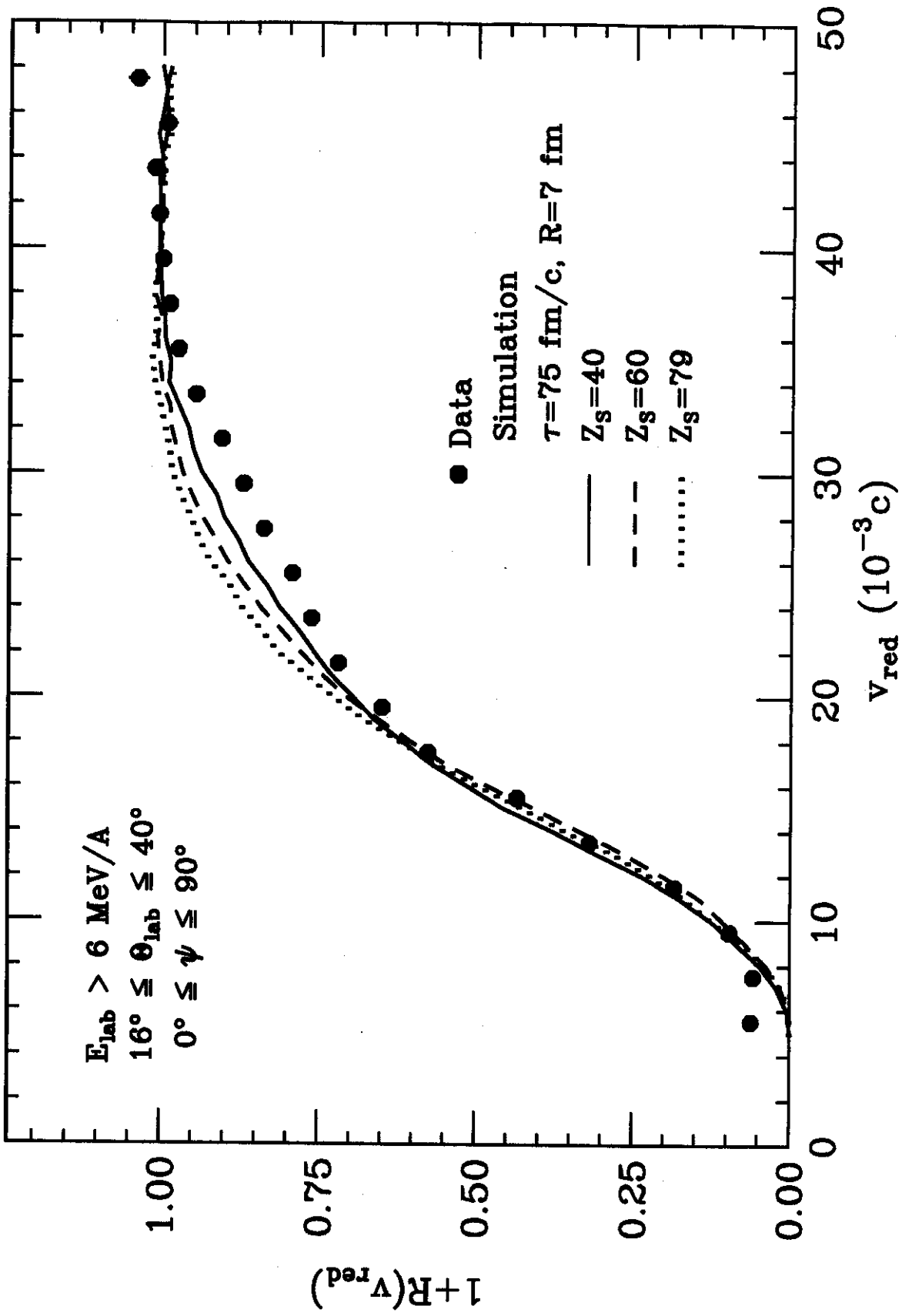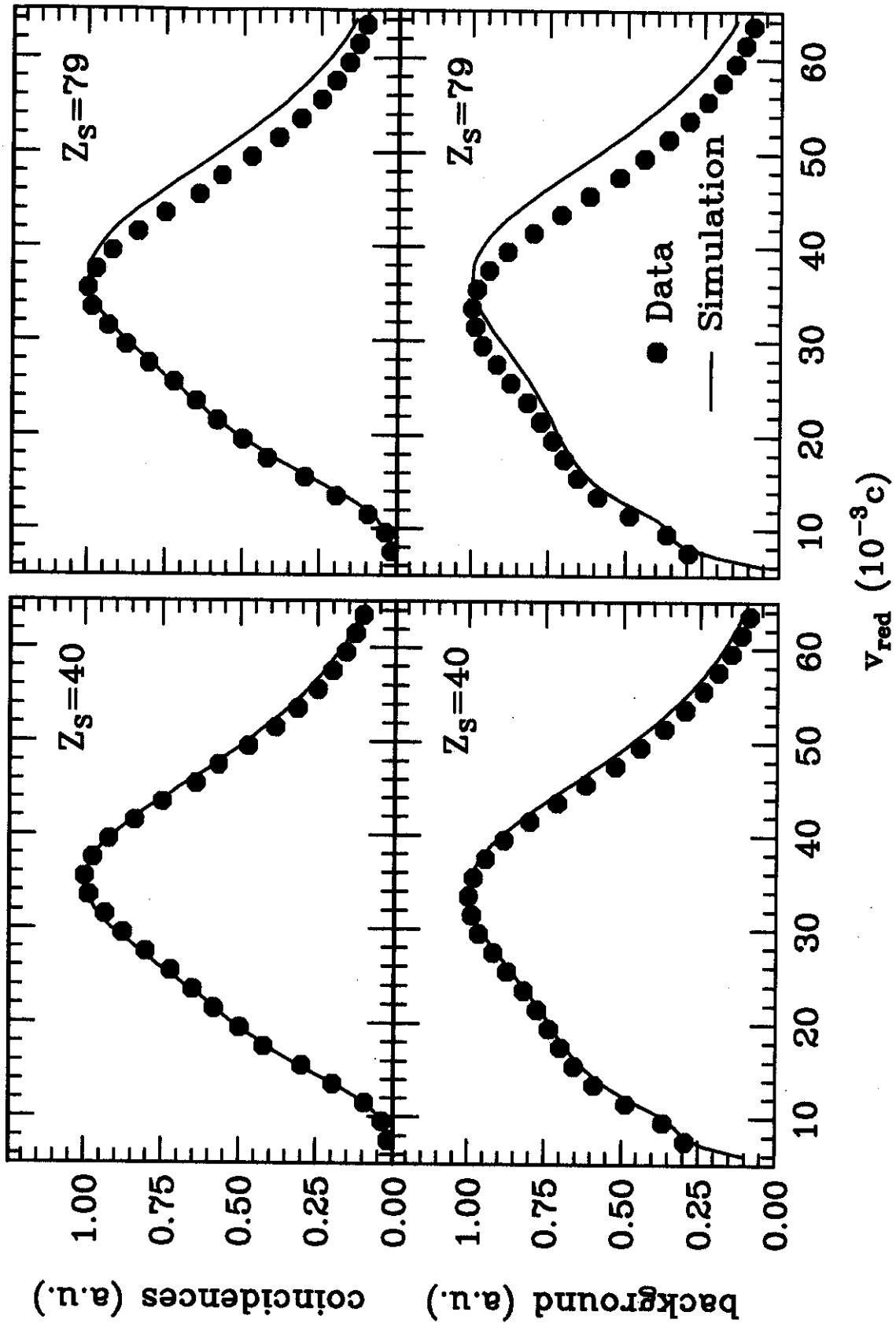
Glasmacher -- Figure 8

Glasmacher – Figure 7

Glasmacher – Figure 8
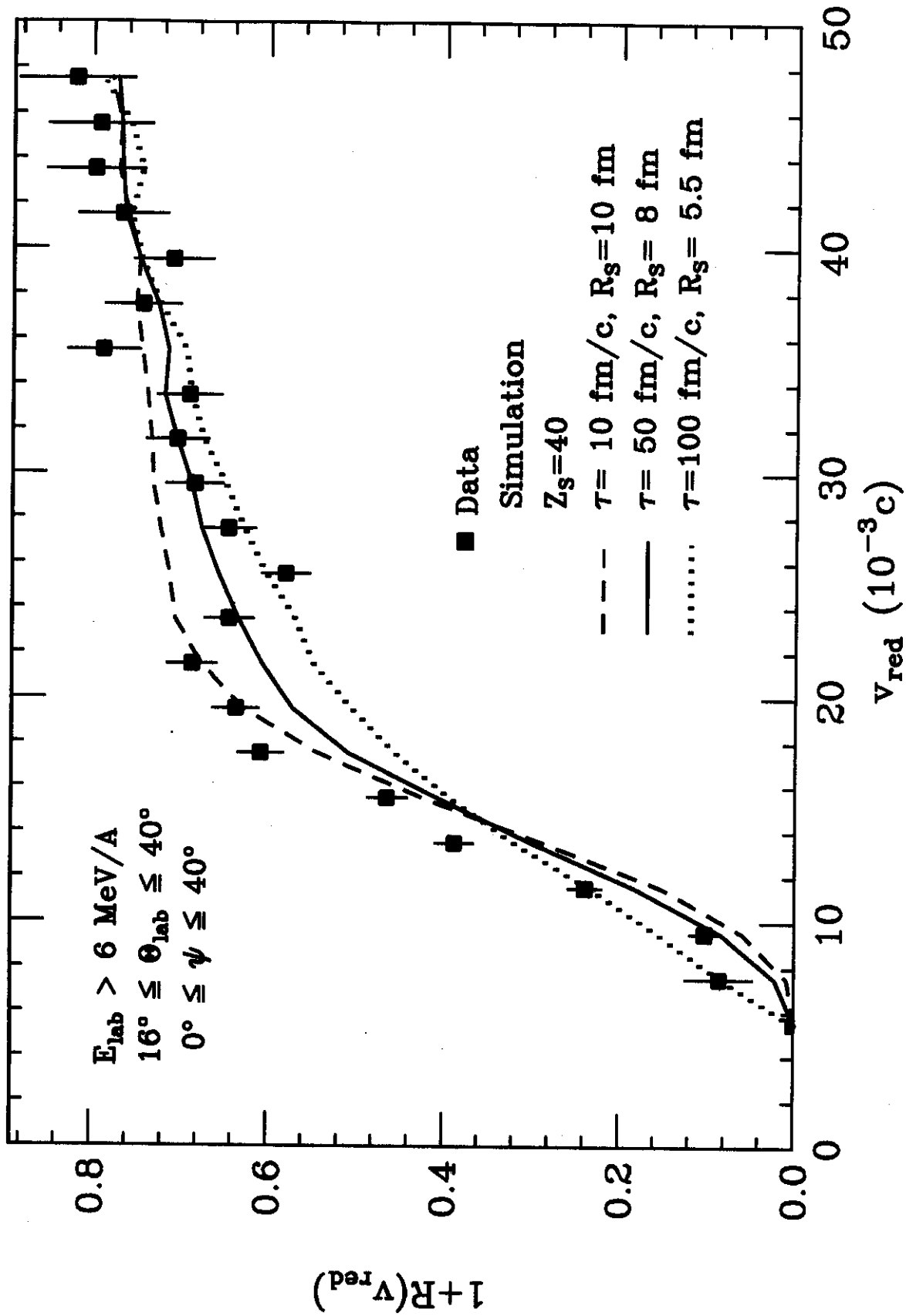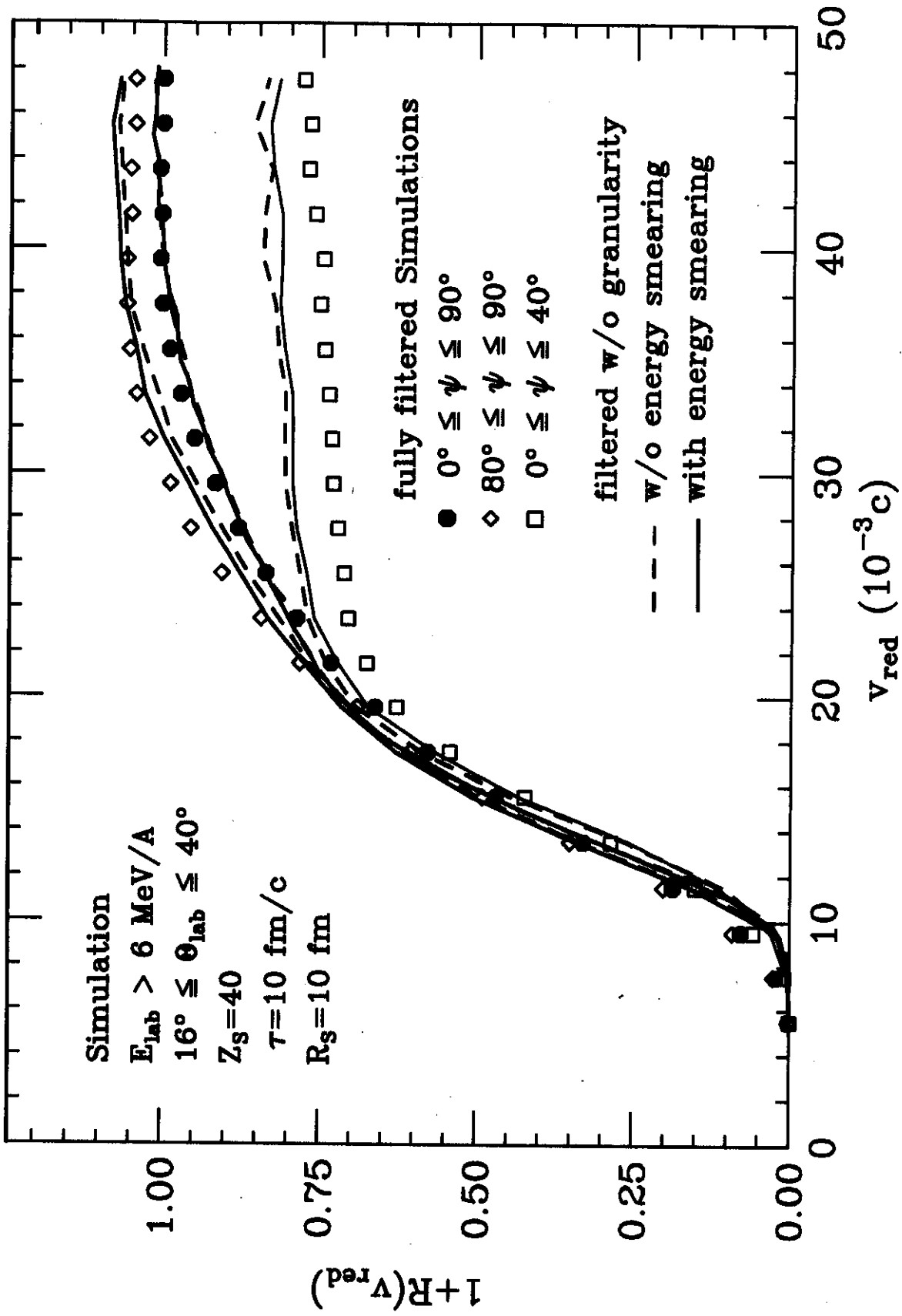
Glasmacher – Figure 10

Glasmacher – Figure 11

Glasmacher – Figure 12

Glasmacher – Figure 13